Discover Applied Sciences

Research

Magnetic hexadecylamine-graphene quantum dots-silver nanoparticle nanocomposite as adsorbents for the removal of phenanthrene and bacteria from aqueous solution

Gugu Kubheka[1] · Adedapo O. Adeola[1] · Ronald Ngulube[1] · Nolwazi Nombona[1] · Patricia B. C. Forbes[1]

Received: 24 April 2024 / Accepted: 7 August 2024
Published online: 02 September 2024

Abstract
In this study, novel multifunctional magnetic silver nanoparticles complexed with hexadecylamine-functionalized sulfur- and nitrogen-co-doped graphene quantum dots (AgNPs@Fe_3O_4-C_{16}SNGQDs) were tested for the removal of phenanthrene and as antibacterial agents from an aqueous solution. The resulting materials were successfully applied as adsorbents and antibacterial agents in batch adsorption and disk diffusion tests. An average Brunauer–Emmett–Teller (BET) surface area of 83.7 and 85.3 m^2/g was obtained for AgNPs@Fe_3O_4 and AgNPs@Fe_3O_4-C_{16}SNGQDs, respectively. Accordingly, adsorption capacity evaluated using the Langmuir adsorption isotherm was found to be 4097.7 and 5965.7 mg/g for AgNPs@Fe_3O_4 and AgNPs@Fe_3O_4-C_{16}SNGQDs, respectively, after 24 h mixing time. The modification of AgNPs@Fe_3O_4 with C_{16}-SNGQDs facilitated higher adsorption performance at ambient temperature, which is more sustainable and cost-effective when considering large-scale use. Furthermore, C_{16}-SNGQDs showed increased antibacterial activity against negatively charged bacterial strains, whereas AgNPs@Fe_3O_4-C_{16}SNGQDs showed enhanced inhibition against gram-positive bacteria. Hence, multifunctional nanoparticles have the potential for microbial and chemical pollution remediation and could significantly improve current water treatment methods.

Keywords Antimicrobial test · Disk diffusion · Adsorption · Phenanthrene · Iron oxide · Silver nanoparticle · Hexadecylamine graphene quantum dots

1 Introduction

Numerous toxic organic and inorganic species are potentially generated at industrial and agricultural sites, and aromatic compounds are one of the most ubiquitous classes of organic contaminants produced by anthropogenic activities as a result of industrialization and urbanization [1–4]. Therefore, removal of aromatic compounds from water sources has become an essential area of research for sustainable development [5]. Aromatic compounds, such as polycyclic aromatic hydrocarbons (PAHs), pose a risk to living organisms because of their mutagenicity, carcinogenicity, toxicity, and bioaccumulation [6–8]. The major contributors to PAHs in water include the burning of coal,

Supplementary Information The online version contains supplementary material available at https://doi.org/10.1007/s42452-024-06147-y.

✉ Gugu Kubheka, gugukhathide@gmail.com; Adedapo O. Adeola, adedapo.adeola@aaua.edu.ng; Ronald Ngulube, ronaldngulube@gmail.com; Nolwazi Nombona, nolwazi.nombona@up.ac.za; Patricia B. C. Forbes, patricia.forbes@up.ac.za | [1]Department of Chemistry, Faculty of Natural and Agricultural Sciences, University of Pretoria, Lynnwood Road, Hatfield, Pretoria 0002, South Africa.

wood, biofuel, and biomass as well as vehicle emissions [9]. According to the US EPA (USA Environmental Protection Agency), 16 PAHs have been classified as pollutants, including phenanthrene, which is used as a model PAH in this context [10, 11]. Regular monitoring of PAHs in the environment and more research on low-cost and improved techniques are recommended [12].

The hydrophobic nature and π-conjugation characteristics of PAHs have been focal points in the development and design of new separation techniques for the removal of these pollutants from water. Various techniques have been developed in this regard and among these is the adsorption method which has been widely researched [5, 7, 8]. The interest in this technique has been motivated by its ease of operation, simplicity, low waste production, ability to remove most water pollutants, and high process efficiency [13, 14]. The nature of the analyte determines the choice of adsorption technique. Different adsorption mechanisms include electrostatic interactions, H-bonding, hydrophobic interactions, H-bonding, acid–base interactions, coordination, π-complexation, and π-π interactions [15–17]. Some conventional adsorbents used in adsorption techniques are limited to weak interactions, such as van der Waals and electrostatic interactions, which limits their application in water treatment [18]. To address this issue, research has focused on developing new sorbents that can form chemical complexes through the formation of weak chemical bonds.

The advantage is that the weak bonds formed through chemical complexation are easily reversible and stronger than the van der Waals interactions [19]. Transition metals such as Ag can form π-complexes (a subclass of chemical complexation) with unsaturated hydrocarbons. This adsorption technique has been primarily used for the removal and separation of ethylene from paraffin, aromatics from gasoline, and trace amounts of butadiene from butene [20]. Molecular orbital calculations have shown that Cu and Ag form stronger π-complexation bonds with thiophene than with benzene [21].

In our previous work, C_{16}SNGQDs was employed as an efficient adsorbent for the removal of phenanthrene from aqueous solutions, with a high adsorption efficiency of 1377 mg/g at 25 °C. However, isolating these nanomaterials from water is challenging because of their high dispersibility. Therefore, the introduction of Fe_3O_4 nanoparticles can contribute to better material performance and enhance the practical application of these materials as samplers, sorbents, and catalysts [22, 23]. Furthermore, modified Fe_3O_4 nanoparticles have been used as environmentally friendly separation methods for the removal of heavy metal ions [24–27] and organics [26, 28, 29].

Metal-based nanoparticles provide a non-antibiotic approach to inactivate microorganisms. Nanoparticles have been proven to be a potential alternative for controlling microorganisms resistant to conventional antibiotics [30, 31]. Their mechanism of action is completely different from that described for traditional antibiotics, which target multiple biomolecules, thereby compromising the development of resistant strains [30]. The antibacterial activity of metal-based nanoparticles, such as AgNPs and Fe_3O_4, has been intensively explored because of their small size compared with bacteria, large specific surface area, and dimensional control. In addition, a smaller dosage of these nanoparticles can provide effective, targeted, and broad-spectrum antibacterial activity [32].

Moreover, GQDs have also been employed as antibacterial agents because of their quantum size effect and oxygen-containing functional groups, which cause them to produce more oxidative stress effects that kill bacteria [33]. The multifunctional capability of the C_{16}SNGQDs has not yet been evaluated. Therefore, this study aimed to synthesize and characterize a novel multifunctional nanoparticle based on iron oxide coated with APTES-functionalized silver nanoparticles complexed with hexadecylamine-functionalized graphene quantum dots for potential remediation of microbial and chemical pollution as shown in Scheme 1.

The main objectives were to improve the adsorption properties of C_{16}SNGQDs reported by our group [34] and extend their properties as antibacterial agents by (i) incorporating Fe_3O_4 nanoparticles for ease of separation and enhanced surface adsorption; (ii) functionalization of Fe_3O_4 with APTES groups to improve the reactive sites for complexation with AgNPs, which are known antibacterial agents; (iii) use of AgNPs as an antibacterial agent and to link C_{16}SNGQDs to the magnetic complex; (vi) evaluate the adsorption capacity of the two adsorbents, namely AgNPs@Fe_3O_4 and AgNPs@Fe_3O_4-C_{16}SNGQDs to establish the optimum conditions for efficient water remediation applications using fluorescence spectroscopy to measure the adsorption efficiency and predict the nature of the sorbate-sorbent interaction; and (v) explore the antibacterial properties of C_{16}SNGQDs, AgNPs@Fe_3O and AgNPs@Fe_3O_4-C_{16}SNGQDs against *P. aeruginosa* CB1 a Gram-negative strain, and *B.subtilis* CN2, a gram-positive strain. The adsorptive materials were synthesized and then characterized using microscopic techniques {transmission electron microscope (TEM) and scanning electron microscope (SEM)}, Raman and X-ray diffraction (XRD) spectroscopy, Fourier transform infrared (FTIR) spectroscopy, energy-dispersive X-ray spectroscopy (EDS), dynamic light scattering (DLS), and Brunauer–Emmett–Teller (BET) analysis.

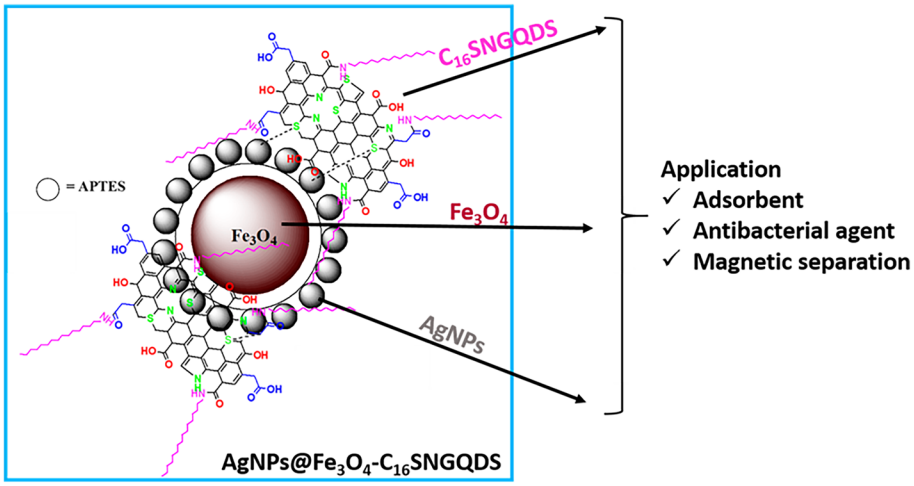

Scheme 1 Schematic representation of the synthesized multifunctional nanoparticles and proposed applications

2 Experimental procedure

2.1 Materials

Iron (II) sulfate heptahydrate ($FeSO_4{\cdot}7H_2O$), iron (III) chloride ($FeCl_3$), (3-aminopropyl)triethoxysilane (3-APTES), silver nitrate ($AgNO_3$), tryptic soybean broth, and polyvinylpyrrolidone (PVP) were purchased from Sigma-Aldrich. Ethylene glycol, sodium hydroxide, toluene, anhydrous ethanol (EtOH), dimethylformamide (DMF), methanol (MeOH), calcium chloride, and sodium azide were obtained from Associated Chemical Enterprises. Deionized water from a Milli-Q water purification system (Millipore, Bedford, MA, USA) was used to prepare all solutions. Supelco supplied phenanthrene standard (≥ 98% purity). The synthesis of SNGQD was reported in [29]. Antibacterial studies were carried out using *Pseudomonas aeruginosa* CB1 and *Bacillus subtilis* CN2, Gram-negative and Gram-positive bacterial strains, respectively, which were previously isolated at the University of Pretoria [35].

2.2 Synthesis of magnetic hexadecyl-graphene quantum dots nanocomposite

2.2.1 Synthesis of magnetite nanoparticles

Magnetite nanoparticles were synthesized at room temperature by chemical co-precipitation of Fe^{3+} and Fe^{2+} according to a procedure described in the literature [36]. NaOH was used as the precipitation agent. A solution containing 0.02 mol $FeCl_3$ and 0.01 mol $FeSO_4{\cdot}7H_2O$ were dissolved and degassed in DI water, and the mixture was sonicated for 15 min. Thereafter, under nitrogen, a degassed solution of 0.08 M NaOH was added dropwise to the reaction mixture with stirring to form a black precipitate, which was further stirred for 3 h. The precipitate was washed several times with DI water and ethanol. The particles were separated from the supernatant by centrifugation followed by vacuum drying at 80 °C for 6 h.

2.2.2 Synthesis of 3-APTES functionalised magnetite nanoparticles

Functionalisation was done following a procedure reported in the literature [37]. Fe_3O_4 (3 g) was dispersed in toluene (30 mL) by sonication for 10 min under ambient conditions. Subsequently, 6 mL of 3-APTES was added dropwise to the Fe_3O_4 suspension, and the reaction solution was mixed for 12 h under reflux at 110 °C. The product was separated from the supernatant by centrifugation with 80% ethanol followed by vacuum drying for 24 h at 55 °C.

2.2.3 Preparation of silver-magnetite nanoparticles

The immobilization of AgNPs on 3-APTES functionalised Fe_3O_4 was achieved following a previously reported procedure with slight modifications [37]. Briefly, 3 g of 3-APTES functionalised Fe_3O_4 was dispersed in 50 mL deionized H_2O and stirred for 0.5 h followed by the addition of 6 g of PVP as a capping agent, 0.1 mol/L $AgNO_3$ and 30 mL of Ethylene glycol were used as reducing agents. The mixture was refluxed for 1 h at 75 °C.

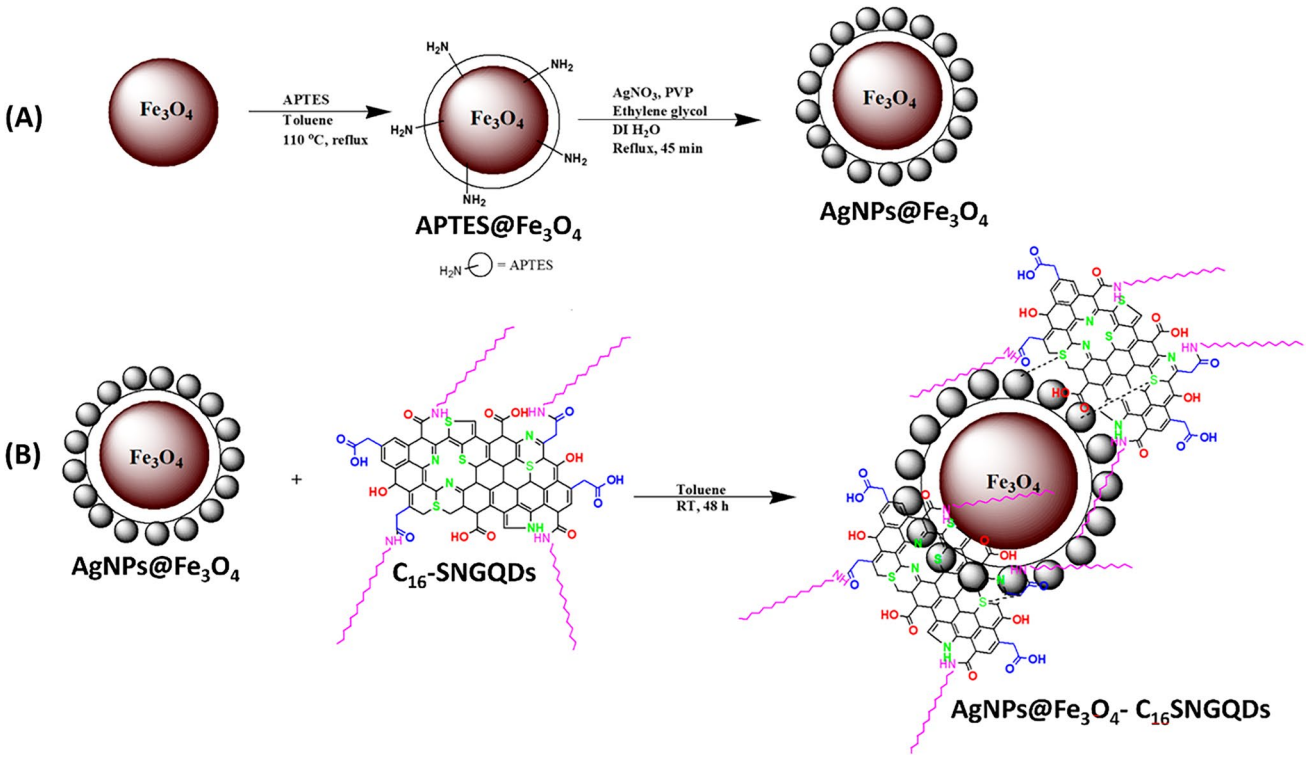

Scheme 2 Structures of the proposed adsorption materials

2.2.4 Synthesis of magnetic graphene quantum dots nanocomposite

The complexation of AgNPs@Fe_3O_4 and C_{16}-SNGQDs was achieved using a slightly modified procedure reported previously [38]. As shown in Scheme 2, a mixture of 0.5 g AgNPs@Fe_3O_4 and 1 g C_{16}-SNGQDs in DMF (35 mL) was sonicated for 4 h at 30 °C. The light-brown solution was further stirred under ambient conditions for 48 h, followed by repeated centrifugation with 80% MeOH for 5 min at 6000 rpm to obtain a pure product.

2.3 Characterisation

Morphological and structural characterizations of the AgNPs@Fe_3O_4-C_{16}SNGQDs, APTES@Fe_3O_4, and AgNPs @Fe_3O_4 were carried out to obtain FTIR spectra using a Bruker Optik spectrometer (Ettlingen, Germany). With a 532 nm excitation laser running at 5 mW power, Raman spectroscopy was performed using a WiTec alpha300 RAS^+ confocal Raman microscope (WiTec, Germany). A Zeiss Ultra-Plus 55 field-emission scanning electron microscope (FE-SEM) equipped with an energy-dispersive X-ray spectrometer (EDS) (Oxford Link-ISIS-300 Zeiss, Germany) and a scanning electron microscope (SEM) were used at a voltage of 2.0 kV. High-resolution transmission electron microscopy (TEM) images were obtained using JEOL JEM 2100F (JOEL Ltd., Tokyo, Japan) operating at 200 kV. Powder X-ray diffraction (XRD) spectra were obtained using a Bruker D2 Phaser with Cu (Kα) radiation (λ = 1.54184 Å) (Bruker AXS GmbH, Karlsruhe, Germany), powder X-ray diffraction (XRD). The adsorption efficiency of the materials was measured using a Yvon Jobin Horiba Fluoromax-4 spectrofluorometer (Edison, New Jersey, USA) at 360 nm excitation and 5 nm slit widths. A Zetasizer Nano ZS (ZEN3600, Malvern,UK) was used to measure the zeta potential and particle size distribution immediately after the dispersion. All zeta potential and size measurements were performed in triplicate and The Quantachrome TouchWin™ software analyser. The NOVA Touch LX6 version was used to measure the nitrogen adsorption and desorption isotherms. All samples were degassed in a high vacuum atmosphere at 77 K for 10 h. Brunauer–Emmett–Teller (BET) method was used to compute the specific surface area from the adsorption isotherms in the relative pressure range (P/P0) of 0.01 to 0.2, and the DFT approach was used to determine the pore size distribution.

2.4 Sorption isotherm study

The study involved batch adsorption of phenanthrene using AgNPs@Fe_3O_4 and AgNPs @Fe_3O_4-C_{16}SNGQDs in 40 mL PTFE screw-cap amber vials at a temperature of 25 ± 1 °C. To suppress microbial activity, the background electrolyte included 200 mg/L of NaN_3 and 0.01 mol/L of $CaCl_2$ in DI water. Phenanthrene was used in isotherm experiments at starting concentrations of 1–30 mg/L. Thermodynamic analyses were conducted in a thermostatic shaking water bath at temperatures ranging from 25 to 45 °C [39].

2.5 Quantification

After centrifugation for 5 min centrifugation at 6000 rpm, clear supernatants were collected for further studies using fluorescence spectroscopy. Furthermore, fluorescence spectroscopy at an excitation wavelength of 290 nm and emission wavelength of 300 nm was used to determine the concentration of phenanthrene prepared in triplicate (n = 3). The regression coefficient (R2) was determined by obtaining matrix-matched calibration curves for phenanthrene at concentrations ranging from 0.5 to 10 mg/L. The equilibrium concentration (Ce, mg/L) and adsorbed solute (qe, mg/g) were calculated using calibration regression and mass balance equations, respectively [39, 40].

$$q_e = \frac{(C_0 - C_e)V_0}{S_m}, \tag{1}$$

$$\text{Sorption efficiency (\%)} = \frac{(C_0 - C_e)}{C_0} \times 100, \tag{2}$$

where C_e (mg/L) is the equilibrium solute concentration, C_o (mg/L) is the initial concentration, V_o (L) is the initial volume, and S_m (g) is the weight of the sorbent.

2.5.1 Antibacterial tests

The glassware and media were sterilized by autoclaving for 15 min at 121 °C. The antibacterial activities of the C16-SNGQDs, AgNPs@Fe_3O_4, and AgNPs@Fe_3O_4-C_{16}SNGQDs were tested against Gram-negative and Gram-positive bacteria.

2.5.2 Disk diffusion test

Kirby-Bauer disk diffusion test was employed to assess the antibacterial activity of C_{16}-SNGQDs, AgNPs@Fe_3O_4, and AgNPs@Fe_3O_4-C_{16}SNGQDs [41]. Briefly, 100 µL of ~5×10^6 CFU/mL of a bacterial suspension was uniformly spread on the surface of nutrient agar plates. Thereafter, filter paper disks with diameters of 7 and 10 mm were dipped in different concentrations of C_{16}-SNGQDs, AgNPs@Fe_3O_4 or AgNPs@Fe_3O_4-C_{16}SNGQDs and were then placed on the agar surface. After incubating the inverted agar plates at 37 °C for 24 h, the average diameter of the zone of inhibition was measured in millimeters using a ruler.

3 Results and discussion

3.1 Synthesis and characterisation

The co-precipitation method is favored for the synthesis of Fe_3O_4 nanoparticles because of its simplicity and high yield. To enhance the stability, reduce aggregation, and deposit an NH_2-functionalised coating on the Fe_3O_4 nanoparticles, APTES groups were attached through a condensation reaction between the -OH groups on the iron oxide nanoparticles and silanol groups on the silane molecule. The NH_2-groups from APTES were further employed to complex the AgNPs through self-assembly, with PVP and ethylene glycol as the capping and reducing agents, respectively. Moreover, the

high affinity of silver for sulfur and nitrogen permitted further functionalisation of AgNPs @Fe_3O_4 with C_{16}SNGQDs. This was achieved through static interactions between the S and N atoms in the GQDs and Ag, form an AgNPs @Fe_3O_4 -C_{16}SNGQDs complex.

To characterize the Fe_3O_4, APTES@ Fe_3O_4, AgNPs@Fe_3O_4, and AgNPs @Fe_3O_4-C_{16}SNGQDs, transmission electron microscopy (TEM), dynamic light scattering (DLS), Fourier transform infrared spectroscopy (FTIR), X-ray diffraction (XRD), scanning electron microscopy (SEM), and energy-dispersive spectroscopy (EDS) were employed to gain insights into the particle size, surface charge, functional groups, phase composition, crystallite size, morphology, and elemental composition of the materials.

The particle size of the bare iron oxide nanoparticles was measured from the SEM micrographs using the ImageJ software, as shown in Fig. 1a, b. The synthesized iron oxide nanoparticles exhibited enhanced agglomeration, with an average diameter of 49 ± 7 nm and a particle size distribution of 30–65 nm (Fig. 1a). The SEM micrograph in Fig. 1b reveals that the Fe_3O_4 particles are spherical in shape and uniform in size distribution. EDS showed the presence of Fe, O, and S in the Fe_3O_4 nanoparticles at high percentages. A small percentage of S was observed, which was attributed to the incomplete removal of SO_4^{2-} from $FeSO_4.7H_2O$ (Fig. 1c).

Furthermore, upon coating with APTES, the particle size distribution decreased to a range of 11–45 ± 5 nm (Fig. 2a). The interaction between the Fe_3O_4 nanoparticles was restricted owing to the hydrophobic nature of the organic silica layer, and hence, the size distribution. The TEM micrographs of AgNPs@Fe_3O_4 show a uniform size distribution of the spherical silver nanoparticles with particle sizes ranging from to 4–8 ± 0.5 nm (Fig. 2b). The small size has been attributed to the increased interaction between PVP and the metal particles, which further increases the ability of PVP to stabilize the metal particles, thus resulting in smaller nanoparticles [42]. The strong affinity of Ag for nitrogen in APTES@ Fe_3O_4 permits the formation of the shell. As depicted in the magnified TEM micrograph of APTES@ Fe_3O_4 in Fig. 2c, a thick incomplete shell was formed.

Figures 2d and 3a show TEM micrographs of the composite. The micrographs show polydispersed GQDs with a size distribution of 2–12 nm and mean diameter of 7.8 nm on the agglomerated Fe_3O_4 surface (Fig. 3). DLS measurements were conducted in deionized water (pH ≈ 6.8) to determine the surface charges and particle sizes of the prepared materials. This confirmed an increase in the particle size of the AgNPs@Fe_3O_4 and AgNPs@Fe_3O_4-C_{16}SNGQD from 349 and 705 nm, respectively. The zeta potential revealed a slightly positive surface charge for all materials. C_{16}SNGQDS showed greater colloidal stability with a zeta potential of 28.8 mV compared to AgNPs@Fe_3O_4 and AgNPs@Fe_3O_4-C_{16}SNGQDs with 19.1 and 18.5 mV zeta potentials, respectively (Figure S1–S3, Supporting Information). This could be due to the superparamagnetic properties of the Fe_3O_4 nanoparticles.

Furthermore, the adsorption of phenanthrene to AgNPs@Fe_3O_4 and AgNPs @Fe_3O_4-C_{16}SNGQDs resulted in a further decrease in zeta potential to -10.5 and 16.6 mV, respectively. DLS measurements revealed an increase in the particle size upon the adsorption of phenanthrene on AgNPs@Fe_3O_4 to 870 d.nm and AgNPs @Fe_3O_4-C_{16}SNGQDs to 742 d.nm. The increase in particle size could explain the increase in colloidal instability.

SEM micrographs of APTES@Fe_3O_4, AgNPs@Fe_3O_4, and AgNPs @Fe_3O_4 -C_{16}SNGQDs are shown in Fig. 4a–c. The micrographs reveal a decrease in agglomeration with increasing modification of the Fe_3O_4 surface, which was also confirmed by TEM micrographs. All the materials were predominantly semi-spherical. EDS analysis of these semi-spherical particles confirmed the expected elements. The presence of Si, Ag, and S peaks, in addition to Fe_3O_4 peaks, confirms the successful grafting of APTES and subsequent functionalization with AgNPs and C_{16}SNGQDs to form APTES@Fe_3O_4, AgNPs@

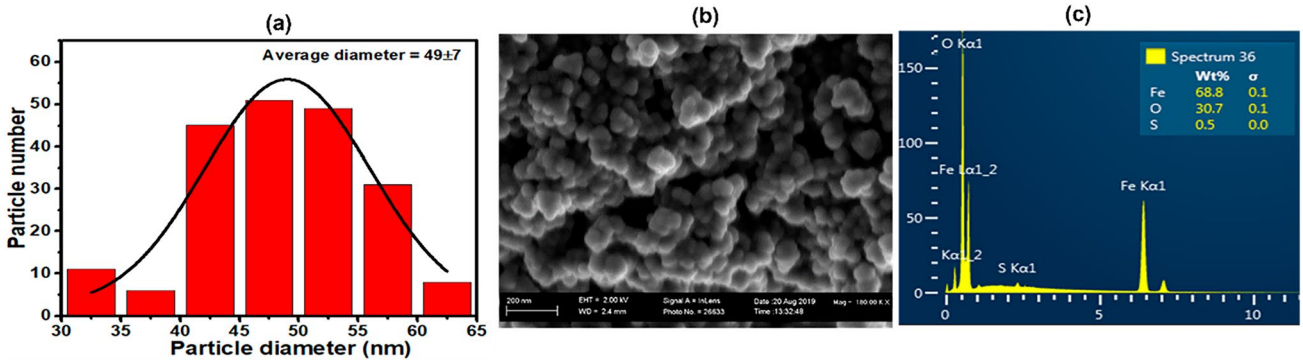

Fig. 1 **a** Particle size distribution histogram calculated from the SEM micrograph, **b** SEM micrograph, and (**c**) EDS spectrum of bare Fe_3O_4

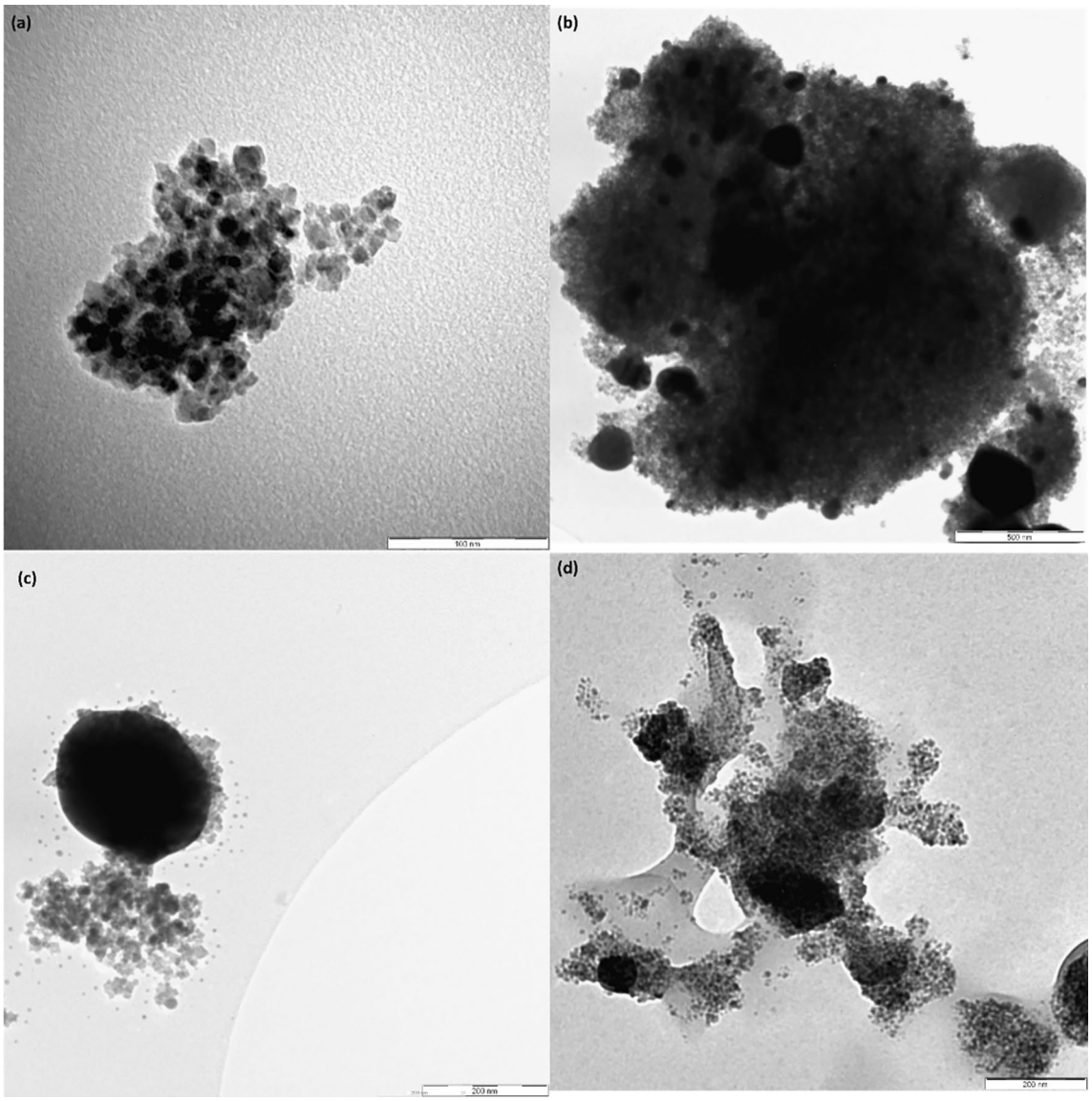

Fig. 2 Micrographs of (**a**) APTES@ Fe_3O_4, (**b**) AgNPs@Fe_3O_4, (**c**) high magnification TEM micrographs of AgNPs@Fe_3O_4, and (**d**) AgNPs @ Fe_3O_4-C_{16}SNGQDs

Fe_3O_4, and AgNPs@Fe_3O_4-C_{16}SNGQDs, respectively (Fig. 4d–f). There was also a decrease in the Fe and O peaks as Fe_3O_4 surface modification increased. The Al peak was attributed to the aluminium stubs used during preparation, and the sample layer may have been too thin (Fig. 4f). Na and Cl peaks were only observed in the EDS spectrum of APTES, which could be due to incomplete washing. Further purification of AgNPs@Fe_3O_4 and AgNPs @Fe_3O_4-C_{16}SNGQDs completely removed the NaCl salt (Fig. 4d–f).

The FTIR spectra of bare Fe_3O_4, APTES@Fe_3O_4, C_{16}-SNGQDs, AgNPs@Fe_3O_4 and AgNPs @Fe_3O_4-C_{16}SNGQDs are shown in Fig. 5. The peaks located at 3379, 1632, 627, and 541 cm^{-1} represent the absorption bands of the OH stretch, OH bend, Fe^{2+}–O, and Fe^{3+}–O stretching, respectively [43], as shown in Fig. 5a (bottom). These peaks were also observed in the IR spectra of APTES@Fe_3O_4, AgNPs@Fe_3O_4, and AgNPs@Fe_3O_4-C_{16}SNGQDs. The presence of these absorption bands indicates the presence of Fe_3O_4 in these materials. The peak at 1359 cm^{-1} ascribed to S=O could be due to the $FeSO_4.7H_2O$ used as a precursor in the synthesis. This peak disappeared from the IR spectra of the other materials owing to the increased number of washing stages.

Furthermore, in the IR spectrum of APTES@Fe_3O_4, peaks located at ca. The 2926, 1559, 1483, 1382, 1328, 1111, and 1011 cm^{-1} represent the absorption bands of the CH_2 stretching vibrations of the anchored amino-propyl group, NH_2–CH_2–Si, CH_2-Si wagging, Si–C–H bending, and aliphatic C–N and Si–O, respectively [44–46] (Fig. 5a, top). These peaks

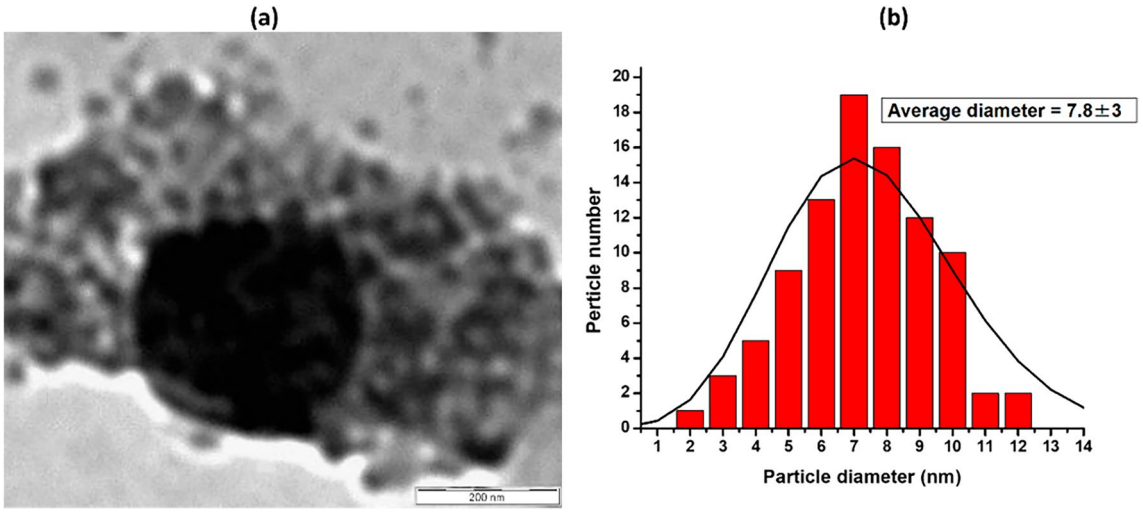

Fig. 3 **a** High-magnification TEM micrograph of AgNPs@Fe_3O_4-C_{16}SNGQDs to show the particles on the surface of Fe_3O_4 and (**b**) size distribution of C_{16}SNGQDs on the Fe_3O_4 surface

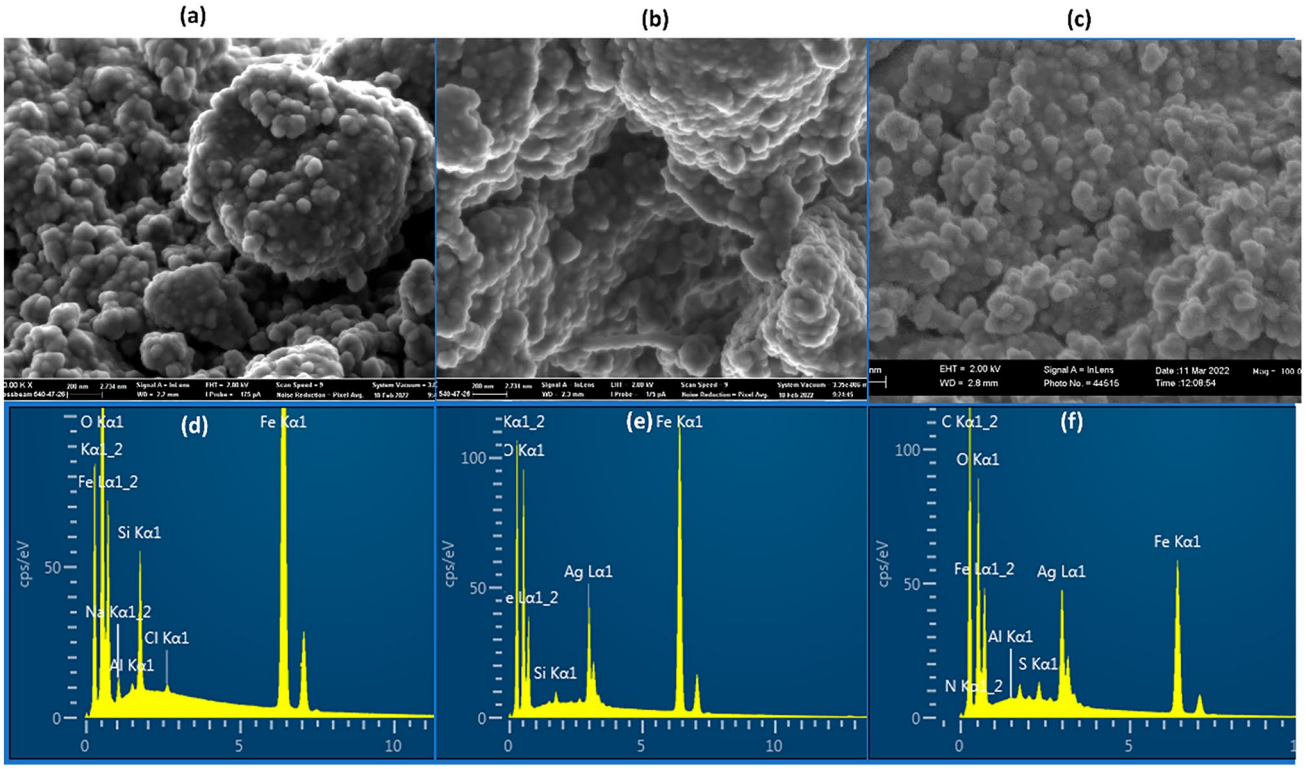

Fig. 4 SEM micrograph of (**a**) APTES@Fe_3O_4, (**b**) AgNPs@Fe_3O_4, (**c**) AgNPs@Fe_3O_4-C_{16}SNGQDs and EDS spectra of (**d**) APTES@Fe_3O_4, (**e**) AgNPs@Fe_3O_4, (f) AgNPs@Fe_3O_4-C_{16}SNGQDs

also appeared in the FTIR spectra of AgNPs@Fe_3O_4 and AgNPs@Fe_3O_4-C_{16}SNGQDs and were absent in the IR spectrum of bare Fe_3O_4. This confirmed the successful functionalization of Fe_3O_4 with APTES. The presence of functional groups at 1640 and 1376 cm^{-1} corresponding to C=O and CH bonds in PVP in the IR spectra of AgNPs@Fe_3O_4 confirmed the presence of PVP-functionalized AgNPs [47] (Fig. 5b, top).

A detailed IR analysis of the C_{16}-SNGQDs was previously reported by our group [34] (Fig. 5b, middle). The IR spectrum of the AgNPs@Fe_3O_4-C_{16}SNGQDs showed CH_3, CH_2, C=O, C=C, and C–O–C peaks at 2915, 2847, 1797, 1647, and 1063 cm^{-1}, respectively, which can be attributed to the presence of C_{16}SNGQDs. Additionally, the absorption bands observed in AgNPs@

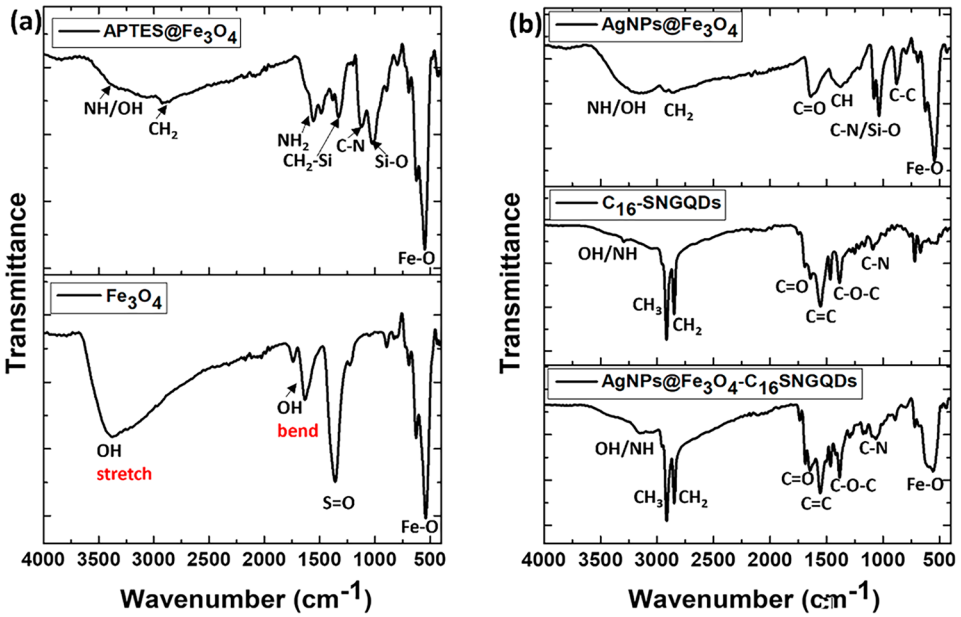

Fig. 5 FTIR spectra of the precursors and the composite

Fe_3O_4, particularly the Fe–O band, appeared in the FTIR spectrum of the composite. The shifts in the Fe^{3+}–O absorption bands observed in the FTIR spectra from 541 cm^{-1} (Fe_3O_4), 546 cm^{-1} (APTES@Fe_3O_4), and 548 cm^{-1} (AgNPs@Fe_3O_4) to 558 cm^{-1} (AgNPs@Fe_3O_4-C_{16}SNGQDs) indicate the possible coordination of AgNPs and C_{16}SNGQDs with Fe_3O_4. Another shift from 1640 to 1737 cm^{-1} was observed in the C=O stretch upon the addition of C_{16}SNGQDs to form a composite. This shift could be due to the interaction of Ag with the C=O groups in C_{16}SNGQDs [47, 48].

The XRD spectrum of Fe_3O_4 shown in Fig. 6a depicts the characteristic diffraction peaks marked with black dotted lines at 2θ = 30.1°, 35.5°, 43.1°, 53.4°, 57.0°, and 62.6°, representing the (220), (311), (400), (422), (511), and (440) indices, respectively. The modification with Fe_3O_4 decreased the intensity of these characteristic diffraction peaks owing to the shielding effect of the grafted materials and the diffraction peak of the amorphous C_{16}SNGQDs (Fig. 6a–e). The blue dotted lines in Fig. 6 represent three diffraction peaks at 38.1°, 64.4°, and 77.6° corresponding to the (111), (220), and (311) indices, respectively, which match well with the standard silver values (JCPDS No. 04-07830) [49]. Furthermore, the sharp peak at 21° in the XRD pattern of the C_{16}SNGQDs corresponds to hexadecylamine (Fig. 6e). The presence of these peaks in the AgNPs@Fe_3O_4-C_{16}SNGQDs confirmed the successful synthesis of the composite (Fig. 6d).

The Raman spectrum of the composite shows two dominant peaks at ca. 1400 cm^{-1} and 1574 cm^{-1}, which are assigned to the D- and G-bands, respectively (Fig. 6, right). The minor decrease in the intensity of the D-band of the C_{16}SNGQDs upon complexation indicates that the materials become more crystalline and less defective [34]. Furthermore, according to Yan et al. [50], the redshift of the G-band is associated with mechanical compression. In this study, the redshift in the Raman spectrum of the C_{16}SNGQDs was attributed to the functionalization with AgNPs@Fe_3O_4. The extent of the structural defects on the surface of the C_{16}SNGQDs upon complexation with AgNPs@Fe_3O_4 was determined by the D-band and G-band (I_D/I_G) ratios calculated using their relative intensities. The I_D/I_G ratio of the C_{16}SNGQDs decreased from 1.52 to 0.70 in the composite. This is attributed to the increase in the amount of disorder upon the interaction of the heteroatoms in the graphene sheet with the sp^3 hybrised AgNPs@Fe_3O_4.

3.2 Adsorption studies

Adsorption remains one of the most widely utilized techniques for the decontamination of polluted water, and isotherms facilitate an understanding of the sorption mechanisms, binding strength, adsorption capacity, and efficiency of various adsorbents [34, 51]. Several models were employed in this study to elucidate the experimental data, including linear (Eq. 3), Freundlich (Eq. 4), Langmuir (Eq. 5) and Sips model (Eq. 6) (Figs. 7 and 8). The models were validated using the Sum of Squared Errors (*SSE*) (Eq. 6).

$$q_e = K_d C_e. \tag{3}$$

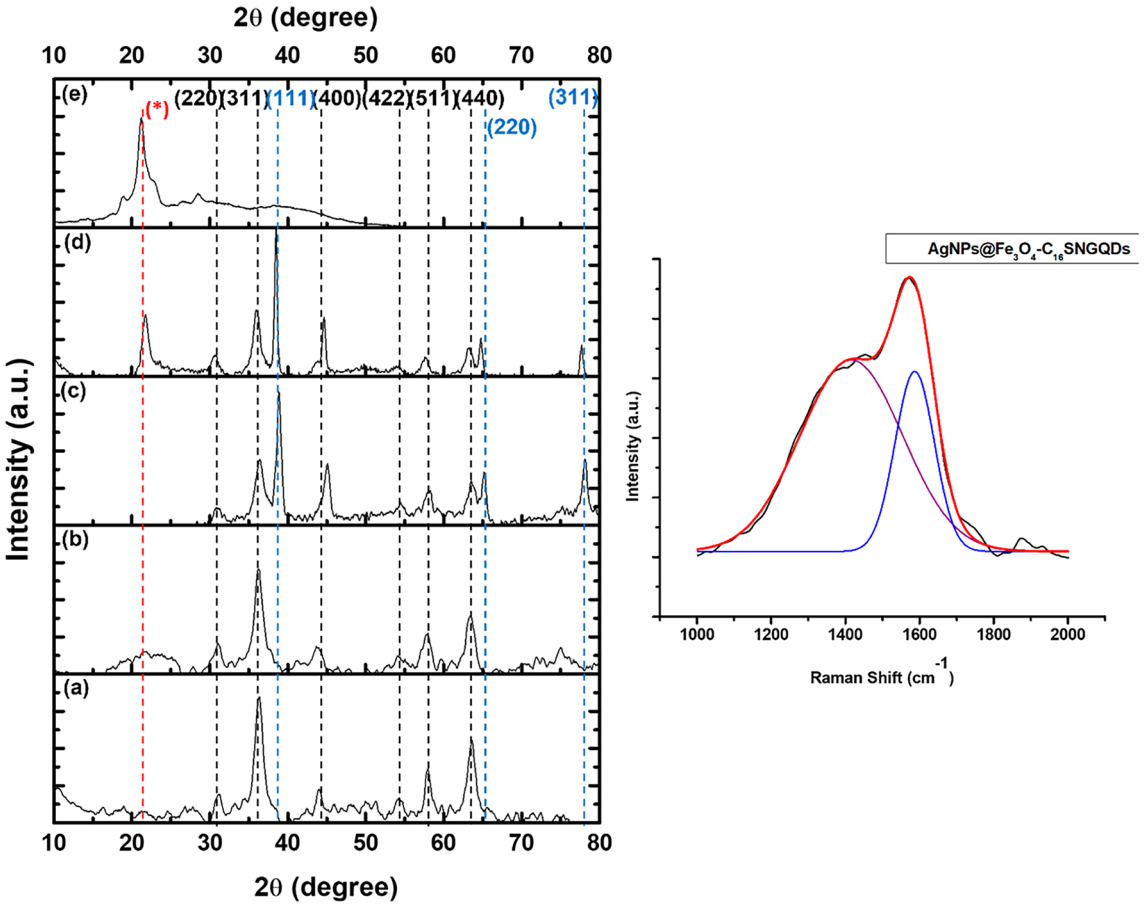

Fig. 6 XRD spectra (left) of (**a**) Fe_3O_4 (**b**) APTES@Fe_3O_4, (**c**) AgNPs@Fe_3O_4, (**d**) AgNPs@Fe_3O_4-C_{16}SNGQDs and (**e**) C_{16}SNGQDs. Raman spectrum (right) of AgNPs@Fe_3O_4-C_{16}SNGQDs

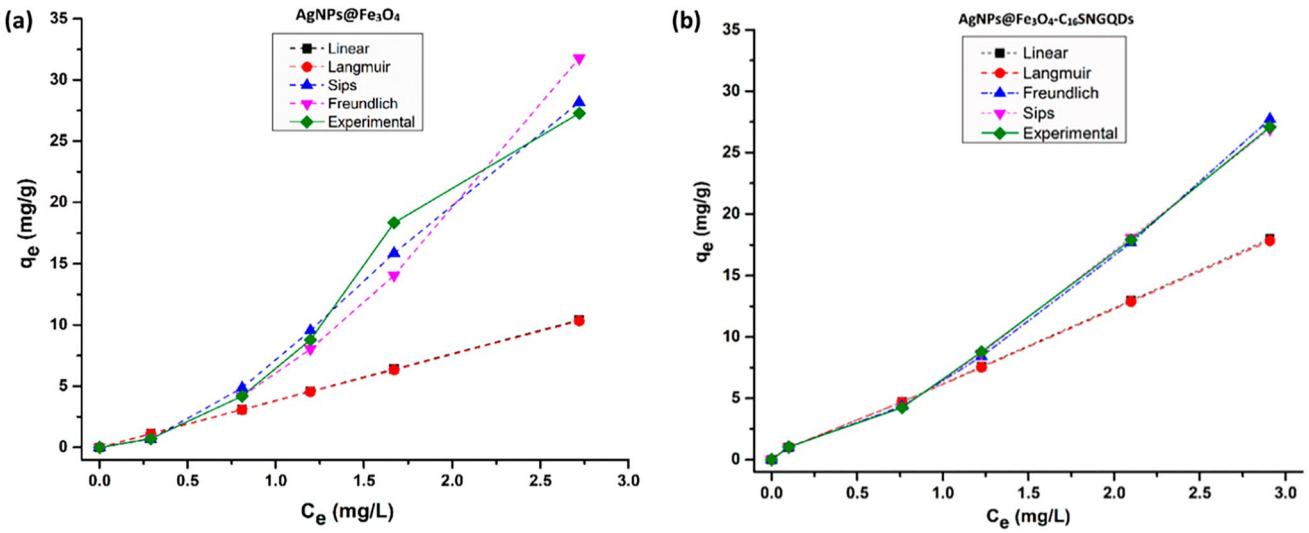

Fig. 7 Phenanthrene adsorption isotherm plots for AgNPs@Fe_3O_4 and AgNPs@Fe_3O_4-C_{16}SNGQDs (adsorption parameters: phenanthrene concentration = 1–30 mg/L; dosage = 5 mg per 5 mL; mixing rate = 200 rpm; T = 25 ± 1 °C; mixing time = 24 h)

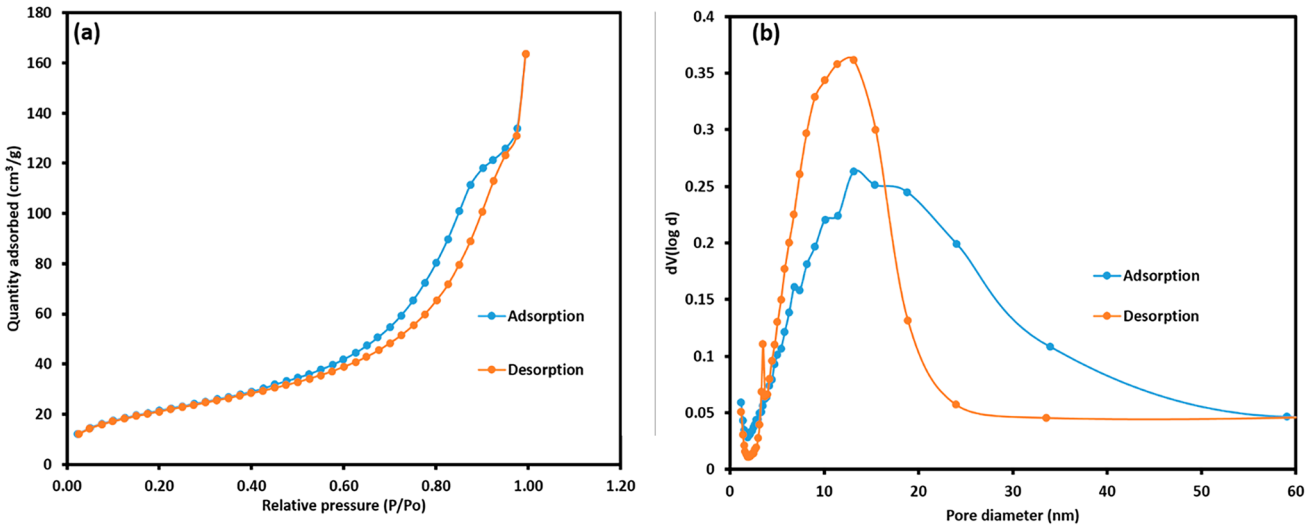

Fig. 8 Adsorption–desorption isotherm plot (**a**) and BJH pore size distribution plot (**b**) of AgNPs@Fe_3O_4

$$q_e = K_F C_e^N. \tag{4}$$

$$q_e = \frac{q_{max} K_L C_e}{1 + K_L C_e}. \tag{5}$$

$$q_e = \frac{q_m K_s C_e^{ms}}{1 + K_s . C_e^{ms}}. \tag{6}$$

$$\sum_{i=1}^{n} (q_{e,cal} - q_{e,exp})_i^2. \tag{7}$$

The variables in the equation are as follows: K_F and N represent the Freundlich constant, which describes the sorption capacity of multiple layers and the heterogeneity indices. q_{max} represents the Langmuir sorption capacity and K_L represents the sorption constant related to the solute-surface interaction energy. K_s and q_m are constants in the Sips model representing the maximum adsorption capacity. ms is the exponent of the Sips isotherm and q_e is the amount of phenanthrene adsorbed. Ce is the equilibrium concentration of phenanthrene and Kd is the adsorption partition coefficient [34, 52].

Compared with the linear forms of isotherm modelling, the nonlinear fitting of the models (Eqs. 3–7) used to ascertain the sorption mechanism between PAH and the synthesized adsorbents is more accurate [53, 54]. The Sips model best fits the data obtained from the experiments on phenanthrene adsorption by AgNPs@Fe_3O_4 and AgNPs@Fe_3O_4-C_{16}SNGQDs, considering the isotherm data and SSE values. (Table 1). The Sips model (Langmuir and Freundlich models combined) is frequently used [53]. Thus, the interactions of phenanthrene with AgNPs@Fe_3O_4 were highly heterogeneous, with comparatively high heterogeneity (*N* and m_s) indices of 1.674 and 1.977, respectively (Table 1). This is consistent with the more heterogeneous and rougher surface morphology shown in Fig. 4 for AgNPs@Fe_3O_4.

The phenanthrene sorption interaction with AgNPs@Fe_3O_4-C_{16}SNGQDs leans towards multiple layers of adsorption (Freundlich), rather than a single layer of adsorption (Langmuir), based on the *SSE* values. Because of restrictions on the amount of sorbate and solute properties, single-mechanism models, such as the Freundlich and Langmuir models, cannot fully explain the interaction of phenanthrene with nanocomposites. However, the Freundlich model may replace the Sips model, depending on the alterations in the amount of contaminants and surface interactions between phenanthrene and the synthesized adsorbents [34].

Table 1 Isotherm data for adsorption of phenanthrene onto functionalized GQDs nano-sorbents

Sorption models	Adsorption parameters		
		AgNPs@Fe_3O_4	AgNPs@Fe_3O_4-C_{16}SNGQDs
	K_F	5.951	6.344
Freundlich	N	1.674	1.381
	SSE	***0.0937***	***0.0033***
Langmuir	q_{max} *(mg/g)*	4097.7	5965.7
	K_L *(L/mg)*	9.29e-4	1.03e-3
	SSE	***1.437***	***1.958***
Linear	K_d	3.829	6.177
	SSE	***1.435***	***1.956***
Sips	K_s	0.150	0.073
	q_m *(mg/g)*	54.179	93.979
	m_s	1.977	1.592
	SSE	***0.0265***	***0.0004***

The adsorption parameters that determine the model are in bold and italics

3.3 Adsorption isotherms

3.3.1 BET analysis

The surface area, pore volume, and pore diameter of the AgNPs@Fe_3O_4 and AgNPs@Fe_3O_4-C_{16}SNGQDs were determined using N_2 adsorption–desorption isotherms at 77 K, and the results are shown in Fig. 8 and Table 2. The prepared adsorbents exhibited desorption hysteresis type IV adsorption–desorption isotherms, which indicate a mesoporous material. An average BET surface area, pore volume, and pore diameter of 83.7 m^2/g, 0.2515 cc/g, and 7.46 nm were calculated for AgNPs@Fe_3O_4, respectively. In contrast, the AgNPs@Fe_3O_4-C_{16}SNGQDs exhibited average BET surface areas, pore volumes, and pore diameters of 85.1 m^2/g, 0.2545 cc/g, and 10.52 nm, respectively. Compared to the C_{16}SNGQDs, the total pore volume and surface area of the AgNPs@Fe_3O_4-C_{16}SNGQDs were significantly improved after iron modification.

3.3.1.1 Effect of temperature Several biological, chemical, and physical processes are strongly affected by the temperature. The Van't Hoff equations (Eqs. 8 and 9) were used to determine the adsorption thermodynamic parameters such as the change in entropy (ΔS), enthalpy (ΔH), and Gibbs free energy (ΔG). Equation 3 was used to obtain the sorption equilibrium constant (K_d) for varying temperatures and for the Van't Hoff plot (Fig. 9):

$$\ln K_d = \frac{\Delta S^\circ}{R} - \frac{\Delta H^\circ}{RT}, \tag{8}$$

$$\Delta G^\circ = -RT \ln K_d, \tag{9}$$

where R is the gas constant (8.314 J/mol K) and T is the thermodynamic temperature (K) [55].

Table 2 BET Parameters calculated from nitrogen adsorption–desorption isotherm for AgNPs@Fe_3O_4 and AgNPs@Fe_3O_4-C_{16}SNGQDs

Material	BET surface area (m^2/g) adsorption	BET surface area (m^2/g) desorption	BJH Pore volume (cc/g) adsorption	BJH Pore volume (cc/g) desorption	BJH Pore diameter (nm) adsorption	BJH Pore size (nm) desorption
AgNPs@Fe_3O_4	78.473	88.838	0.247	0.256	6.813	8.121
AgNPs@Fe_3O_4-C_{16}SNGQDs	80.015	90.113	0.250	0.259	9.792	11.254

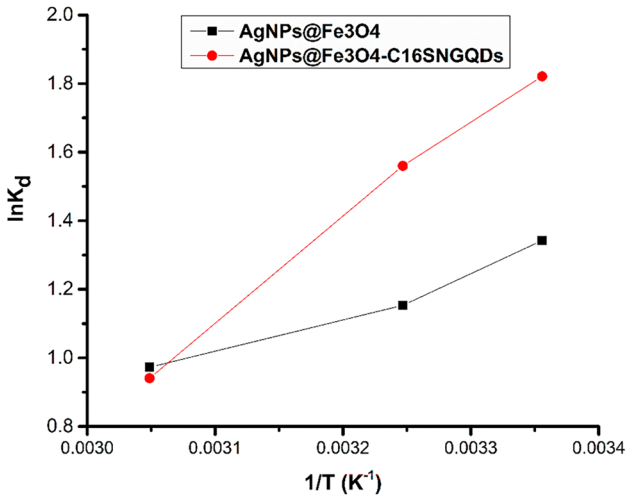

Fig. 9 Van't Hoff plot for phenanthrene sorption by AgNPs@Fe_3O_4 and AgNPs@Fe_3O_4-C_{16}SNGQDs

Table 3 Thermodynamic data for adsorption of phenanthrene by AgNPs@Fe_3O_4 and AgNPs@Fe_3O_4-C_{16}SNGQDs

Sorbents	Temperature	ln K_d	ΔG° (kJ/mol)	ΔH° (kJ/mol)	ΔS° (J/mol.K)
AgNPs@Fe_3O_4	298	1.343	− 3.33	− 9.72	− 21.65
	313	1.153	− 2.95		
	323	0.973	− 2.65		
AgNPs@Fe_3O_4-C_{16}SNGQDs	298	1.821	− 4.51	− 24.11	− 65.60
	313	1.560	− 4.00		
	328	0.941	− 2.57		

Phenanthrene sorption by the AgNPs@Fe_3O_4 and AgNPs@Fe_3O_4-C_{16}SNGQDs was exothermic (Table 3). This negative value confirms the spontaneous adsorption process. Van der Waals interactions form bonds between the sorbent and sorbate when H° is between 5 kJ/mol and 10 kJ/mol, as in the case of AgNPs@Fe_3O_4, which is known as physisorption. The chemical bonding interactions were attributed to the sorption process when $\Delta H°$ was in the range of 30–70 kJ/mol. This type of sorption is known as chemisorption [56]. AgNPs@Fe_3O_4-C_{16}SNGQDs interaction with phenanthrene was neither entirely physical nor chemical, supporting the isotherm findings that the process is governed by a complex mechanism (Sips model). However, chemical adsorption is the main adsorption mechanism [57]. The ΔS° values were similarly negative, indicating that during the adsorption process, the degree of freedom at the solid–liquid interface decreased, but more effectively for the AgNPs@Fe_3O_4-C_{16}SNGQDs (– 65 J/mol K), suggesting the presence of strong binding interactions. This implies that both the adsorbent and adsorbate undergo structural modifications [56].

An increase in temperature improved the maximum adsorption capacity (q_{max}) of phenanthrene by the AgNPs@Fe_3O_4-C_{16}SNGQDs (5965.7 mg/g at 25 °C to 9853.2 mg/g at 45 °C). However, the reverse is the case for AgNPs@Fe_3O_4, with a reduction of q_{max} from 4097.7 mg/g @ 25 °C to 2112.7 mg/g @ 45 °C. The modification of AgNPs@Fe_3O_4 with SNGQDs facilitated higher adsorption performance at ambient temperature, which is more sustainable and cost-effective for large-scale applications.

3.3.2 Proposed adsorption mechanism

As shown in Scheme 3, in addition to the expected π–π and hydrophobic interactions between the π-conjugated surface of GQDs and hydrophobic hexadecylamine with phenanthrene, respectively, π-complexation is expected to occur between phenanthrene and the AgNPs through dual bonding. The antibonding π*-orbital of phenanthrene interacts with the outer d-orbital of Ag because Ag becomes more positive owing to the highly electronegative nitrogen in polyvinylpyrrolidone (PVP) used to stabilize the AgNPs. The vacant outermost s-orbital of positively charged Ag may also form a σ-bond with the π-orbitals of phenanthrene. Moreover, PAHs have more conjugative and stronger σ-bonds than single aromatic compounds and thus can easily form σ-bonds with electron acceptors [18].

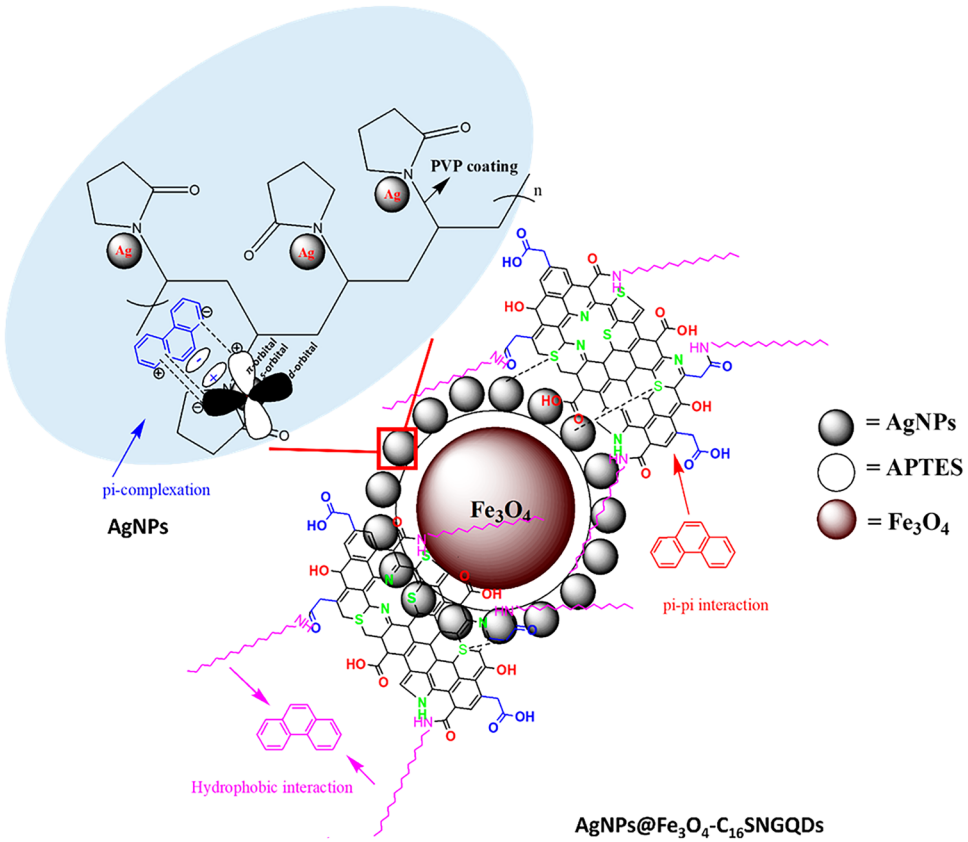

Scheme 3 Schematic representation of possible adsorption mechanisms between phenanthrene and AgNPs@Fe_3O_4-C_{16}SNGQDs

Table 4 Comparison of different materials used for the removal of phenanthrene from aqueous solutions

Material	q_{max} (mg/g) @25°C	Mixing time (h)	References
AgNPs@Fe_3O_4	4097.7	24	This work
AgNPs@Fe_3O_4-C_{16}SNGQDs	5965.7	24	This work
C_{16}SNGQDs	1377	24	[34]
Magnetic graphene oxide	13.65	24	[58]
Magnetic chemically-reduced graphene	30.12	24	[58]
Magnetic annealing-reduced graphene	26.18	24	[58]
Single-walled carbon nanotubes	50.53	5 days	[59]
Charcoal supported 27 titanate nanotubes	12.1	3	[60]
Fe_3O_4-SiO_2-2DMDPS	47.315	10	[61]
Fe_3O_4-SiO_2	34.679	10	[61]
Activated carbon from orange rind	70.92	1.5	[62]
Graphene wool	127	24	[52]
Magnetic multi-walled carbon nanotubes	28.46–20.00	5	[63]
Magnetic single-walled carbon nanotubes	74.61	5	[63]
Magnetic graphene nanosheets	31.53	5	[63]

Table 4 shows that compared to other carbon-based nanocomposites included in Table 4 and published in the literature [34, 58–63], the nanocomposites developed in this study as a bi-functional material had a greater maximum adsorption capacity (q_{max}) derived from the Langmuir isotherm model. This could be explained by the material's morphology and functional groups, hydrophobicity, abundance of π-electrons, and other physicochemical characteristics. Furthermore, the successes recorded in terms of antibacterial properties make the material even more unique as a remediation tool.

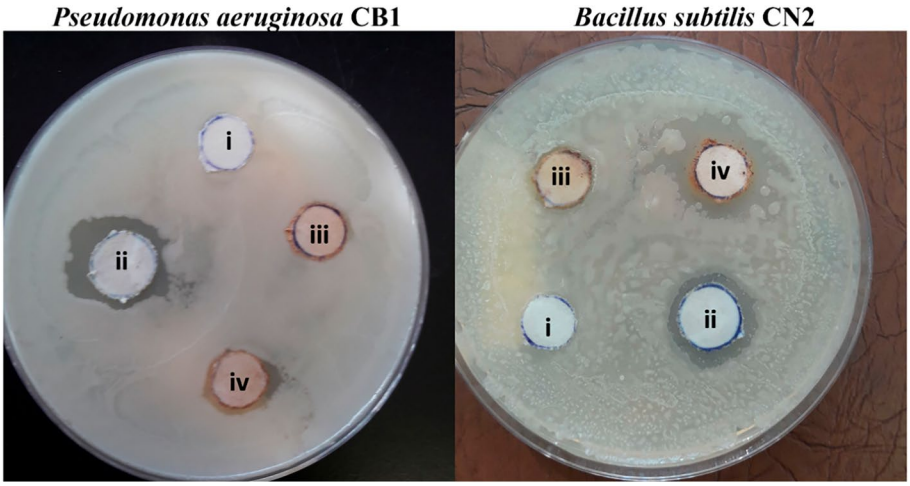

Fig. 10 Representative images of agar plates showing (i) control, (ii) C_{16}SNGQDs, (iii) AgNPs@Fe_3O_4, and iv) AgNPs@Fe_3O_4-C_{16}SNGQDs impregnated disks revealing inhibition zones (ZOI) of Gram-positive *Bacillus subtilis* CN2 and Gram-negative *Pseudomonas aeruginosa* CB1 strains at 4 mg/mL disk dosages of all materials

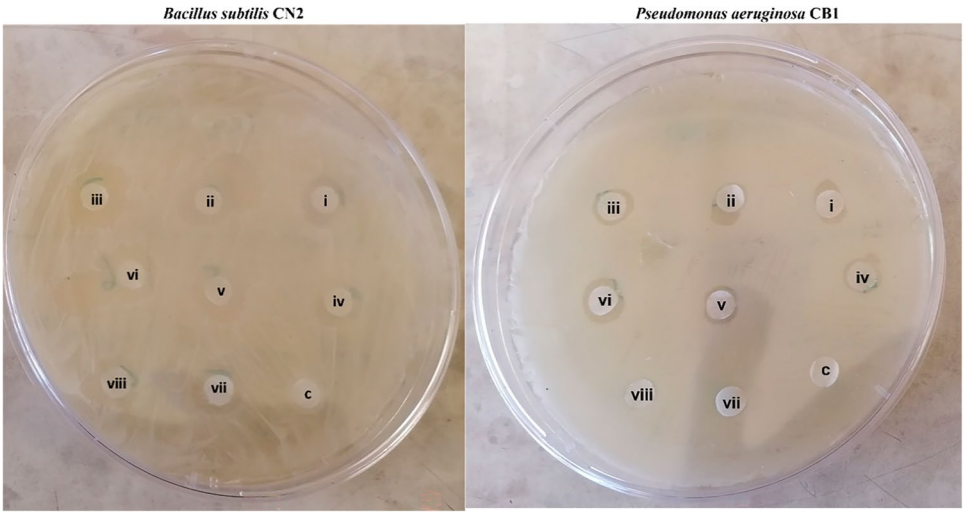

Fig. 11 Representative images of agar plates showing (i) 1000**,** (ii) 500, (iii) 250, (iv) 125, (v) 62.5, (vi) 31.25, (vii) 15.62, (vii) 7.81, and (c) 0 (control) µg/mL impregnated disks revealing the inhibition zones (ZOI) of the composite

3.4 *Bacteria* studies

The antibacterial properties of C_{16}-SNGQDs, AgNPs@Fe_3O_4, and AgNPs@Fe_3O_4-C_{16}SNGQDs were tested against Gram-negative and Gram-positive strains using the disk diffusion method, as shown in Figs. 10 and 11. The diameters of the zones of growth inhibition (in mm) produced by the three tested materials after incubation at 35 °C for ~ 24 h are shown in Fig. 12. All the materials showed antibacterial activity. Filter paper with a diameter of 10 mm was used to compare the antibacterial activities of the different materials (Fig. 10). For the eight concentration studies, a smaller filter paper measuring 7 mm was used (Fig. 11). Deionized water was used as a control, and no bacterial inhibition was observed. As shown in Fig. 11, the hexadecylamine-functionalized GQDs showed a notable zone of inhibition (ZOI) against gram-negative bacteria, followed by the composite and silver-coated iron oxide nanoparticles with ZOI of 21 ± 0.7, 19 ± 0.5, and 11 ± 0.1 mm, respectively.

In a dose-dependent study, the zone of inhibition increased as the concentration of the test materials increased. The studied concentrations ranged from 7.81 to 1000 µg/mL (Fig. 12). AgNPs@Fe_3O_4-C_{16}SNGQDs and C_{16}SNGQDs displayed clear antibacterial activity against both strains, even at lower dosages, whereas AgNPs@Fe_3O_4 showed no antibacterial activity up to 125 µg/mL. According to Bezza et al. and Xiu et al., agglomeration adversely affects the antibacterial activity of a material and may result in no antibacterial activity [35, 64]. This could explain the lack of antibacterial activity of the AgNPs@Fe_3O_4. Furthermore, silver and GQDs composites have been reported to exhibit synergistic effects, resulting in excellent antibacterial activity [41]. The reduced antibacterial activity of AgNPs@Fe_3O_4-C_{16}SNGQDs could be due to agglomeration.

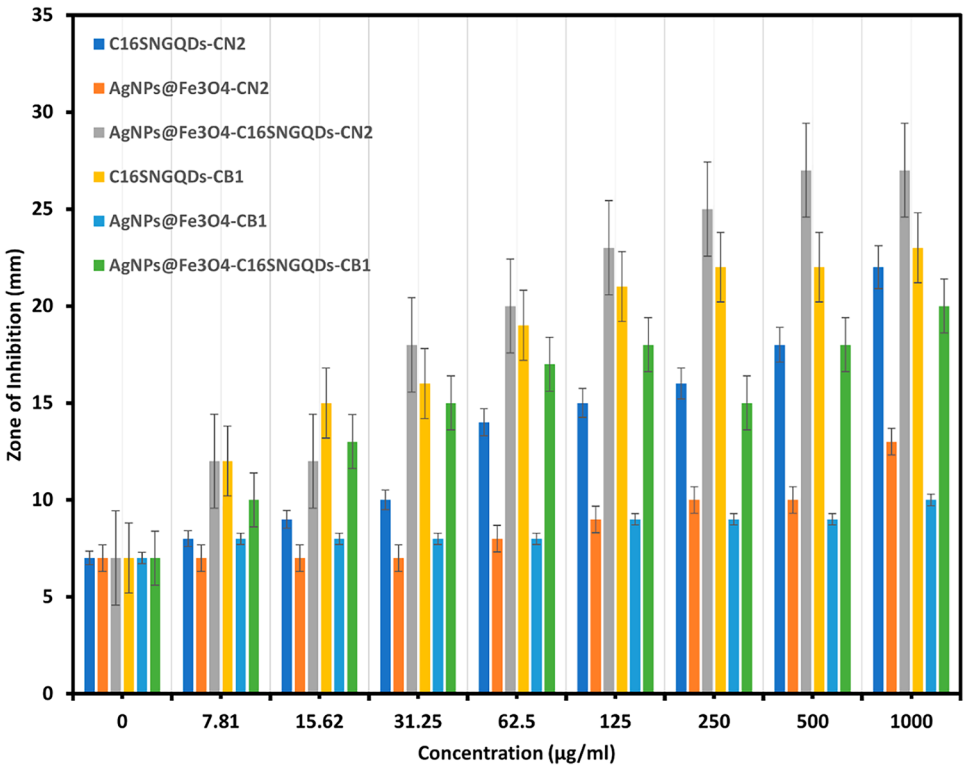

Fig. 12 Changes in the zone of inhibition with varying concentrations of C_{16}SNGQDs, AgNPs@Fe_3O_4, and AgNPs@Fe_3O_4-C_{16}SNGQDs were tested against Gram-negative and Gram-positive bacterial strains at 4 mg/mL disk dosages

3.4.1 Proposed antibacterial mechanism for the materials

Many studies have been performed on the mechanism of action of nanoparticles, but the exact mechanism is still not well understood [38, 65, 66]. As shown in Scheme 4, two pathways are proposed for the antibacterial mechanism of the studied materials. The first pathway involved the dissociation of AgNPs and Fe_3O_4 from the complex and the release of Ag^+ and Fe^{3+} ions from AgNPs@Fe_3O_4 and AgNPs@Fe_3O_4-C_{16}SNGQDs. Nanoparticles and their ions can encircle the outer cell wall, and some can penetrate bacteria through the porin protein. The accumulation of ions on the cell membrane changes its osmotic pressure of the cell membrane, resulting in the loss of nutrients and inactivation of cells. In contrast, ions inside the cell disrupt bacterial DNA and denature proteins, resulting in changes in the bacterial components, thus making the bacteria inactive and resulting in apoptotic cell death.

The second pathway involves the antibacterial effect of GQDs and Fe_3O_4 from C_{16}SNGQDs, AgNPs@Fe_3O_4, and AgNPs@Fe_3O_4-C_{16}SNGQDs which could mainly be caused by the increase in intracellular reactive oxygen species (ROS) levels, that is, H_2O_2, OH^- and O_2^-. A large number of active free radicals can be generated around the cells by the influence of the oxygen-containing functional groups in the GQDs and Fe_3O_4. The accumulation of active free radicals can increase ROS levels in cells and generate large amounts of toxic oxygen species. Excessive accumulation of these species is toxic to bacteria and results in cell death. Synergistic antibacterial effects occur when antibacterial agents encounter bacteria, which results in apoptosis.

In addition, research on the nature of the interactions between different functional groups on bacterial and nanoparticle surfaces revealed that Gram-positive and Gram-negative bacterial cell walls have a net negative charge [67]. Therefore, the enhanced antibacterial activity of C_{16}SNGQDs against both the Gram-positive and Gram-negative bacterial strains can be attributed to the electrostatic interaction between the positively charged C_{16}SNGQDs and the negative charge of the cell component, resulting in membrane stress in the bacterial cell. The bacterial membrane is damaged and ions are released into the cell, which enhances cytotoxicity, resulting in cell death [67].

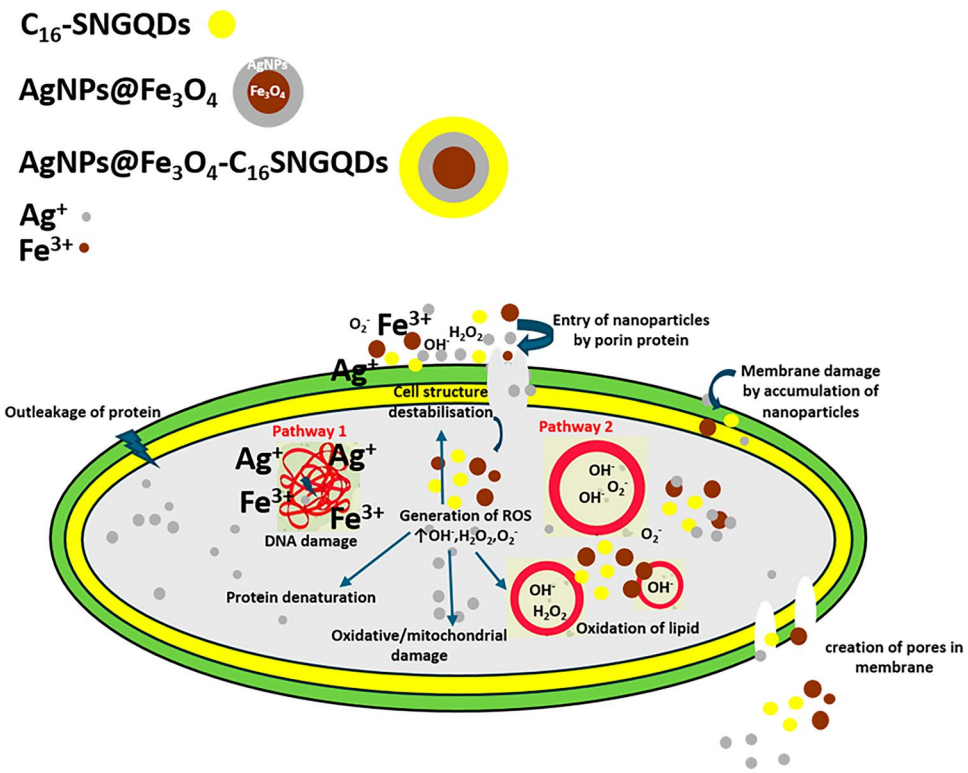

Scheme 4 Schematic representation of the proposed antibacterial mechanism of the materials

4 Conclusion

The C_{16}SNGQDs were successfully complexed with AgNPs@Fe_3O_4 to form the AgNPs@Fe_3O_4-C_{16}SNGQDs nanocomposite. Different characterization techniques confirmed the successful fabrication of the proposed materials. The nanocomposite exhibited excellent adsorption capabilities, and the Sips model best fit the batch data obtained for phenanthrene adsorption by AgNPs@Fe_3O_4 and AgNPs@Fe_3O_4-C_{16}SNGQDs with respect to the isotherm data and SSE values. The phenanthrene sorption interaction with AgNPs@Fe_3O_4-C_{16}SNGQDs leans towards multiple sorption layers (Freundlich), rather than single-layer sorption (Langmuir), considering the *SSE* values. Phenanthrene sorption onto AgNPs@Fe_3O_4 and AgNPs@Fe_3O_4-C_{16}SNGQDs was exothermic and spontaneous based on the negative $\Delta G°$. The maximum sorption capacity improved with an increase in temperature from 5965.7 mg/g @ 25 °C to 9853.2 mg/g @ 45 °C for AgNPs@Fe_3O_4-C_{16}SNGQDs, whereas a reduction in q_{max} from 4097.7 mg/g @ 25 °C to 2112.7 mg/g @ 45 °C was observed in the case of AgNPs@Fe_3O_2. Therefore, the modification of AgNPs@Fe_3O_4 with C_{16}-SNGQDs facilitated a higher adsorption performance at ambient temperature, which is more sustainable and cost-effective. Furthermore, the q_{max} of C_{16}-SNGQDS was significantly improved from 1377 mg g^{-1}. The antibacterial activity of the materials exhibited a high zone of inhibition for C_{16}-SNGQDs against Gram-negative bacteria, AgNPs@Fe_3O_4-C_{16}SNGQDs against Gram-positive bacteria, and AgNPs@Fe_3O_4 displayed little or no inhibition against both strains. Therefore, with appropriate fabrication, C_{16}-SNGQDs and AgNPs@Fe_3O_4-C_{16}SNGQDs can potentially be used as alternative adsorbents for the removal of aromatic hydrocarbon pollutants from water and as antibacterial agents for both Gram-positive and Gram-negative bacteria. Regeneration and reuse of nanocomposites exposed to chemicals and microbes without significantly altering the surface/deactivating material is potentially challenging. Therefore, future studies should investigate the recovery, regeneration, and reuse of this bifunctional nanocomposite, owing to its adsorptive and antibacterial activities.

Acknowledgements Disk diffusion tests and experimental support were provided by Fisseha Bezza and Evans Chirwa. The Rand Water Professorial Chair Program (PF) and University of Pretoria provided funding for this research. The National Research Foundation (NRF) is acknowledged for the postdoctoral fellowship provided to GK (grant number 120777).

Author contributions Gugu Kubheka: Conceptualization, formal analysis, investigation, methodology, writing of the original draft, visualization, and funding acquisition. Adedapo Adeola: formal analysis, investigation, methodology, writing of the original draft, and visualization.

Ronald Ngulube: formal analysis and methodology, Nolwazi Nombona: resources, Patricia Forbes: funding acquisition, project administration, resources, supervision, validation.

Funding This study was funded by The National Research Foundation (NRF) and The Rand Water Professorial Chair program.

Data availability Data are available from the first author upon request.

Declarations

Competing interests The authors declare no competing interests.

References

1. Wang Z, Chen J, Yang P, Tian F, Qiao X, Bian H, Ge LJE. Distribution of PAHs in pine (*Pinus thunbergii*) needles and soils correlates with their gas-particle partitioning. Environ Sci Technol. 2009;43(5):1336–41.
2. Qiao M, Bai Y, Cao W, Huo Y, Zhao X, Liu D, Li ZJC. Impact of secondary effluent from wastewater treatment plants on urban rivers: polycyclic aromatic hydrocarbons and derivatives. Chemosphere. 2018;211:185–91.
3. AL Othman ZA, Badjah AY, Ali IJ. Facile synthesis and characterization of multi walled carbon nanotubes for fast and effective removal of 4-tert-octylphenol endocrine disruptor in water. J Mol Liquid. 2019;275:41–8.
4. Vishnu D, Dhandapani B. A review on the synergetic effect of plant extracts on nanomaterials for the removal of metals in industrial effluents. Curr Anal Chem. 2021;17(2):260–71.
5. Crisafully R, Milhome MAL, Cavalcante RM, Silveira ER, De Keukeleire D, Nascimento RF. Removal of some polycyclic aromatic hydrocarbons from petrochemical wastewater using low-cost adsorbents of natural origin. Biores Technol. 2008;99(10):4515–9.
6. Wang L, Yang Z, Niu J, Wang J. Characterization, ecological risk assessment and source diagnostics of polycyclic aromatic hydrocarbons in water column of the Yellow River Delta, one of the most plenty biodiversity zones in the world. J Hazard Mater. 2009;169(1–3):460–5.
7. Rockne KJ, Shor LM, Young L, Taghon GL, Kosson DS. Distributed sequestration and release of PAHs in weathered sediment: the role of sediment structure and organic carbon properties. Environ Sci Technol. 2002;36(12):2636–44.
8. Maletić SP, Beljin JM, Rončević SD, Grgić MG, Dalmacija BD. State of the art and future challenges for polycyclic aromatic hydrocarbons is sediments: sources, fate, bioavailability and remediation techniques. J Hazard Mater. 2019;365:467–82.
9. Kao TH, Chen S, Chen CJ, Huang CW, Chen BH. Evaluation of analysis of polycyclic aromatic hydrocarbons by the QuEChERS method and gas chromatography–mass spectrometry and their formation in poultry meat as affected by marinating and frying. J Agric Food Chem. 2012;60(6):1380–9.
10. Chen H, Gao G, Liu P, Pan R, Liu X, Lu C. Determination of 16 polycyclic aromatic hydrocarbons in tea by simultaneous dispersive solid-phase extraction and liquid–liquid extraction coupled with gas chromatography–tandem mass spectrometry. Food Anal Methods. 2016;9(8):2374–84.
11. Purcaro G, Moret S, Conte LS. Overview on polycyclic aromatic hydrocarbons: occurrence, legislation and innovative determination in foods. Talanta. 2013;105:292–305.
12. Ejiako EJ, Iheme OU, Okonkwo CU. Persistent organic pollutant: a review on the distribution of polycyclic aromatic hydrocarbons (PAHs) in aquatic ecosystem. Int J Environ Natl Resour. 2022.
13. Sasaki T, Tanaka S. Adsorption behavior of some aromatic compounds on hydrophobic magnetite for magnetic separation. J Hazard Mater. 2011;196:327–34.
14. Mikhail S, Zaki T, Khalil L. Desulfurization by an economically adsorption technique. Appl Catal A. 2002;227(1–2):265–78.
15. Hasan Z, Jhung SH. Removal of hazardous organics from water using metal-organic frameworks (MOFs): plausible mechanisms for selective adsorptions. J Hazard Mater. 2015;283:329–39.
16. Ahmed I, Jhung SH. Adsorptive desulfurization and denitrogenation using metal-organic frameworks. J Hazard Mater. 2016;301:259–76.
17. Vishnu D, Rajendran A, Dhandapani BJE. A potent insight into the microalgal and surface-modified magnetic microalgal biomass synthesis and treatment strategies in the removal of selenium and chromium metal ions. Energy Ecol Environ. 2024;9(2):113–29.
18. Chen J, Yang R. A molecular orbital study of the selective adsorption of simple hydrocarbon molecules on Ag^+- and Cu^+-exchanged resins and cuprous halides. Langmuir. 1995;11(9):3450–6.
19. King CJ. Separation processes based on reversible chemical complexation. New York: Wiley; 1987. p. 760–74.
20. Padin J, Yang RT, Munson CL. New sorbents for olefin/paraffin separations and olefin purification for C4 hydrocarbons. Ind Eng Chem Res. 1999;38(10):3614–21.
21. Yang RT, Takahashi A, Yang FH. New sorbents for desulfurization of liquid fuels by π-complexation. Ind Eng Chem Res. 2001;40(26):6236–9.

22. Sallam S, El-Subruiti G, Eltaweil AJ. Facile synthesis of Ag-γ-Fe_2O_3 superior nanocomposite for catalytic reduction of nitroaromatic compounds and catalytic degradation of methyl orange. Catal Lett. 2018;148:3701–14.
23. Eltaweil AS, Bakr SS, Abd El-Monaem EM, El-Subruiti GM. Magnetic hierarchical flower-like Fe_3O_4@ ZIF-67/CuNiMn-LDH catalyst with enhanced redox cycle for Fenton-like degradation of Congo red: optimization and mechanism. Environ Sci Pollut Res. 2023;30(30):75332–48.
24. Liu J-F, Zhao Z-S, Jiang G-B. Coating Fe_3O_4 magnetic nanoparticles with humic acid for high efficient removal of heavy metals in water. Environ Sci Technol. 2008;42(18):6949–54.
25. Shin S, Jang J. Thiol containing polymer encapsulated magnetic nanoparticles as reusable and efficiently separable adsorbent for heavy metal ions. Chem Commun. 2007;41:4230–2.
26. Bestawy EE, El-Shatby BF, Eltaweil AS. Biotechnology, Integration between bacterial consortium and magnetite (Fe_3O_4) nanoparticles for the treatment of oily industrial wastewater. World J Microbiol Biotechnol. 2020;36(9):141.
27. Vishnu D, Dhandapani B. Synthesis of novel adsorbent by incorporation of plant extracts in amino-functionalized silica-coated magnetic nanomaterial for the removal of Zn^{2+} and Cu^{2+} from aqueous solution. J Environ Health Sci Eng. 2021;19(2):1413–24.
28. Zhao X, Shi Y, Cai Y, Mou S. Cetyltrimethylammonium bromide-coated magnetic nanoparticles for the preconcentration of phenolic compounds from environmental water samples. Environ Sci Technol. 2008;42(4):1201–6.
29. Shan G, Liu H, Xing J, Zhang G, Wang K. Separation of polycyclic aromatic compounds from model gasoline by magnetic alumina sorbent based on π-complexation. Ind Eng Chem Res. 2004;43(3):758–61.
30. Mateo EM, Jiménez M. Silver nanoparticle-based therapy: can it be useful to combat multi-drug resistant bacteria? Antibiotics. 2022;11(9):1205.
31. Sánchez-López E, Gomes D, Esteruelas G, Bonilla L, Lopez-Machado AL, Galindo R, Cano A, Espina M, Ettcheto M, Camins AJN. Metal-based nanoparticles as antimicrobial agents: an overview. Nanomaterials. 2020;10(2):292.
32. Ye L, Cao Z, Liu X, Cui Z, Li Z, Liang Y, Zhu S, Wu S. Noble metal-based nanomaterials as antibacterial agents. J Alloys Compound. 2022;904:164091.
33. Hui L, Huang J, Chen G, Zhu Y, Yang L. Antibacterial property of graphene quantum dots (both source material and bacterial shape matter). ACS Appl Mater Interfaces. 2016;8(1):20–5.
34. Kubheka G, Adeola AO, Forbes PB. Hexadecylamine functionalised graphene quantum dots as suitable nano-adsorbents for phenanthrene removal from aqueous solution. RSC Adv. 2022;12(37):23922–36.
35. Bezza FA, Tichapondwa SM, Chirwa EM. Synthesis of biosurfactant stabilized silver nanoparticles, characterization and their potential application for bactericidal purposes. J Hazard Mater. 2020;393: 122319.
36. Mascolo MC, Pei Y, Ring TA. Room temperature co-precipitation synthesis of magnetite nanoparticles in a large pH window with different bases. Materials. 2013;6(12):5549–67.
37. Salem MA, Elsharkawy RG, Ayad MI, Elgendy MY. Silver nanoparticles deposition on silica, magnetite, and alumina surfaces for effective removal of Allura red from aqueous solutions. J Sol-Gel Sci Technol. 2019;91(3):523–38.
38. Zhang L, Liu L, Wang J, Niu M, Zhang C, Yu S, Yang Y. Functionalized silver nanoparticles with graphene quantum dots shell layer for effective antibacterial action. J Nanopart Res. 2020;22:1–12.
39. Adeola AO, de Lange J, Forbes PB. Adsorption of antiretroviral drugs, efavirenz and nevirapine from aqueous solution by graphene wool: kinetic, equilibrium, thermodynamic and computational studies. Appl Surf Sci Adv. 2021;6: 100157.
40. Ololade IA, Adeola AO, Oladoja NA, Ololade OO, Nwaolisa SU, Alabi AB, Ogungbe IV. In-situ modification of soil organic matter towards adsorption and desorption of phenol and its chlorinated derivatives. J Environ Chem Eng. 2018;6(2):3485–94.
41. Habiba K, Bracho-Rincon DP, Gonzalez-Feliciano JA, Villalobos-Santos JC, Makarov VI, Ortiz D, Avalos JA, Gonzalez CI, Weiner BR, Morell G. Synergistic antibacterial activity of PEGylated silver–graphene quantum dots nanocomposites. Appl Mater Today. 2015;1(2):80–7.
42. Gharibshahi L, Saion E, Gharibshahi E, Shaari AH, Matori KA. Influence of Poly (vinylpyrrolidone) concentration on properties of silver nanoparticles manufactured by modified thermal treatment method. PLoS ONE. 2017;12(10): e0186094.
43. Sharif HMA, Mahmood A, Cheng H-Y, Djellabi R, Ali J, Jiang W-L, Wang S-S, Haider MR, Mahmood N, Wang A-J. Fe_3O_4 nanoparticles coated with EDTA and Ag nanoparticles for the catalytic reduction of organic dyes from wastewater. ACS Appl Nano Mater. 2019;2(8):5310–9.
44. Ma M, Zhang Y, Yu W, Shen H-Y, Zhang H-Q, Gu N. Preparation and characterization of magnetite nanoparticles coated by amino silane. Colloids Surf, A. 2003;212(2–3):219–26.
45. Sahoo M, Singha S, Parida K. Amine functionalized layered double hydroxide: a reusable catalyst for aldol condensation. New J Chem. 2011;35(11):2503–9.
46. Vahedi V, Pasbakhsh P. Instrumented impact properties and fracture behaviour of epoxy/modified halloysite nanocomposites. Polym Testing. 2014;39:101–14.
47. Baganizi DR, Nyairo E, Duncan SA, Singh SR, Dennis VA. Interleukin-10 conjugation to carboxylated PVP-coated silver nanoparticles for improved stability and therapeutic efficacy. Nanomaterials. 2017;7(7):165.
48. Wiley B, Sun Y, Mayers B, Xia Y. Shape-controlled synthesis of metal nanostructures: the case of silver. Chem Eur J. 2005;11(2):454–63.
49. Trang VT, Dinh NX, Lan H, Tam LT, Huy TQ, Tuan PA, Phan VN, Le A-T. APTES functionalized iron oxide–silver magnetic hetero-nanocomposites for selective capture and rapid removal of salmonella enteritidis from aqueous solution. J Electron Mater. 2018;47:2851–60.
50. Yan X, Suzuki T, Kitahama Y, Sato H, Itoh T, Ozaki Y. A study on the interaction of single-walled carbon nanotubes (SWCNTs) and polystyrene (PS) at the interface in SWCNT-PS nanocomposites using tip-enhanced Raman spectroscopy. Phys Chem Chem Phys. 2013;15(47):20618–24.
51. Adeola AO, Abiodun BA, Adenuga DO, Nomngongo PN. Adsorptive and photocatalytic remediation of hazardous organic chemical pollutants in aqueous medium: a review. J Contam Hydrol. 2022;248:104019.
52. Adeola AO, Forbes PB. Assessment of reusable graphene wool adsorbent for the simultaneous removal of selected 2–6 ringed polycyclic aromatic hydrocarbons from aqueous solution. Environ Technol. 2022;43(8):1255–68.
53. Wang J, Guo X. Adsorption isotherm models: classification, physical meaning, application and solving method. Chemosphere. 2020;258: 127279.
54. Adeola AO, Kubheka G, Chirwa EMN, Forbes PBC. Facile synthesis of graphene wool doped with oleylamine-capped silver nanoparticles (GW-αAgNPs) for water treatment applications. Appl Water Sci. 2021;11(11):172.

55. Gupta H, Singh S. Kinetics and thermodynamics of phenanthrene adsorption from water on orange rind activated carbon. Environ Technol Innov. 2018;10:208–14.
56. Chen F-X, Zhou C-R, Li G-P, Peng F-F. Thermodynamics and kinetics of glyphosate adsorption on resin D301. Arab J Chem. 2016;9:S1665–9.
57. Li X, Zhou X, Mu J, Lu L, Han D, Lu C, Wang M. Thermodynamics and kinetics of p-aminophenol adsorption on poly(aryl ether ketone) containing pendant carboxyl groups. J Chem Eng Data. 2011;56(11):4274–7.
58. Huang D, Xu B, Wu J, Brookes PC, Xu J. Adsorption and desorption of phenanthrene by magnetic graphene nanomaterials from water: roles of pH, heavy metal ions and natural organic matter. Chem Eng J. 2019;368:390–9.
59. Yang K, Zhu L, Xing B. Adsorption of polycyclic aromatic hydrocarbons by carbon nanomaterials. Environ Sci Technol. 2006;40(6):1855–61.
60. Liu W, Cai Z, Zhao X, Wang T, Li F, Zhao D. High-capacity and photoregenerable composite material for efficient adsorption and degradation of phenanthrene in water. Environ Sci Technol. 2016;50(20):11174–83.
61. Wei Z, Ma X, Zhang Y, Guo Y, Wang W, Jiang Z-Y. High-efficiency adsorption of phenanthrene by Fe_3O_4-SiO_2-dimethoxydiphenylsilane nanocomposite: experimental and theoretical study. J Hazard Mater. 2022;422:126948.
62. Gupta H. Removal of phenanthrene from water using activated carbon developed from orange rind. Int J Sci Res Environ Sci. 2015;3(7):248.
63. Zhang J, Li R, Ding G, Wang Y, Wang C. Sorptive removal of phenanthrene from water by magnetic carbon nanomaterials. J Mol Liquids. 2019;293:111540.
64. Xiu Z-M, Zhang Q-B, Puppala HL, Colvin VL, Alvarez PJ. Negligible particle-specific antibacterial activity of silver nanoparticles. Nano Lett. 2012;12(8):4271–5.
65. Sportelli M, Izzi M, Volpe A, Clemente M, Picca R, Ancona A, Lugarà P, Palazzo G, Cioffi N. The pros and cons of the use of laser ablation synthesis for the production of silver nano-antimicrobials. Antibiotics. 2018;7(3):67.
66. Prabhu Y, Rao KV, Kumari BS, Kumar VSS, Pavani T. Synthesis of Fe_3O_4 nanoparticles and its antibacterial application. Int Nano Lett. 2015;5:85–92.
67. Patra P, Roy S, Sarkar S, Mitra S, Pradhan S, Debnath N, Goswami A. Damage of lipopolysaccharides in outer cell membrane and production of ROS-mediated stress within bacteria makes nano zinc oxide a bactericidal agent. Appl Nanosci. 2015;5:857–66.